Article

Editor's Pick | Special Collection

Cem Kolbakir (Cem Kolbakır)*, Haiyang Hu (胡海洋), Yang Liu (刘洋) and Hui Hu (胡晖)*

Parametric study on the thermodynamic characteristic of DBD plasma actuations pertinent to aircraft icing mitigation

https://doi.org/10.1515/tp-2026-0073
Received June 9, 2026; accepted July 22, 2026;
published online August 12, 2026

Abstract: Dielectric barrier discharge (DBD) plasma actuators can generate noticeable heating as well as induce momentum to the surrounding flow, which makes them attractive for multifunctional uses such as flow control and anti-/de-icing. In this work, we performed a parametric study to simultaneously quantify both the thermal and mechanical responses of DBD plasma actuation during glow-to-streamer transition. Surface heating was quantified using infrared (IR) thermography, while the actuation-induced thrust was obtained with a high-sensitivity force balance to assess the mechanical output. The measurements indicate that the delivered plasma power varies as a function of key operating and structural material parameters, including the applied voltage, dielectric thickness, and dielectric permittivity. Within the glow-discharge operating state, both heating and thrust scale approximately linearly with the supplied plasma power. When the input power exceeds the glow regime, localized streamer filaments emerge; a larger share of the deposited energy is then released as heat, and the thrust no longer increases. These trends suggest that, in the filamentary mode, energy that would otherwise contribute to mechanical output is increasingly converted into thermal energy.

Keywords: dielectric barrier discharge (DBD); plasma actuators; aircraft icing mitigation; plasma flow control; plasma anti-icing

Article note: This article is part of the Special Collection "Plasmas and Plasma Particles".

***Corresponding authors: Cem Kolbakir (Cem Kolbakır)**, Department of Aerospace Engineering, Samsun University, Samsun, 55420, Türkiye, E-mail: cem.kolbakir@samsun.edu.tr. https://orcid.org/0000-0002-3355-6289; and **Hui Hu (胡晖)**, Department of Aerospace Engineering, Iowa State University, Ames, IA, 50011, USA, E-mail: huhui@iastate.edu. https://orcid.org/0000-0001-7928-4138
Haiyang Hu (胡海洋), Department of Aerospace Engineering, Worcester Polytechnic Institute, Worcester, MA, 01609, USA, E-mail: hhu5@wpi.edu. https://orcid.org/0000-0001-7995-1375
Yang Liu (刘 洋), Department of Mechanical Engineering, The City College of New York, New York, NY, 10031, USA, yliu7@ccny.cuny.edu. https://orcid.org/0000-0003-0289-3837

1 Introduction

Cold-weather operations can compromise flight safety because ice may accumulate on exposed aircraft surfaces. When ice forms on components such as wings and empennage, aerodynamic efficiency deteriorates – drag rises while lift is reduced [1]. Accretion can occur either on the ground or during flight. Green [2] reported 248 ground-icing and 308 in-flight icing incidents between 1982 and 2011. In-flight icing typically develops when supercooled droplets in clouds strike the airframe and freeze upon impact [3]. To limit these hazards, a range of in-flight anti-icing and de-icing approaches has been implemented, including freezing-point depressants [4], pneumatic boots [4], [5], hot-bleed-air systems [4], [6]–[8] and electro-thermal heating [4], [9], [10]. In addition, superhydrophobic coatings have been suggested as a potential anti-icing solution [11]–[13]. Despite these advances, existing methods often do not eliminate ice completely and may introduce new penalties. For instance, pneumatic boots and bleed-air systems can adversely influence aerodynamics, while electro-thermal heaters may melt ice near the leading edge but promote runback ice formation farther downstream along the airfoil.

Beyond the conventional anti-/de-icing approaches noted above, the heat released during plasma generation has recently been proposed as a promising strategy for mitigating icing [14]–[18]. A conventional DBD plasma actuator consists of two offset electrodes separated by a dielectric barrier. When a sufficiently high voltage is imposed between the electrodes, a surface discharge develops and ionizes the air in the vicinity of the dielectric-covered electrode [19]. Broad reviews of DBD plasma actuators as active flow-control devices are available in the works of Moreau

[20] and Corke et al. [21], and Benard et al. [22] provide an overview focusing on the electrical and mechanical characteristics of AC-driven DBD actuators. In addition, Rodrigues et al. [18] present a detailed review specifically addressing DBD plasma actuators for icing mitigation.

DBD plasma actuators can impart momentum to the surrounding flow with very rapid response and without relying on any moving components. This distinctive feature has made DBD plasma a major focus in flow-control research over the past two decades. Applying a high-voltage excitation – either AC or nanosecond-pulsed – initiates a discharge across the electrode pair [19], [20]. In AC-driven DBD operation, the body force responsible for actuation arises from electrohydrodynamic interactions, effectively converting electrical input into fluid motion. The resulting "electric wind" entrains nearby air and produces a wall-jet-like flow, which is exploited for reducing drag, stall-delay control and lift enhancement [19], [20], [23]–[25]. For the cases with nanosecond pulses (ns-DBD), induced ultrafast gas heating generate shockwave which is the main mechanism for flow control [26]–[28].

In addition to generating an induced wall jet, plasma actuation also releases heat. Zhang et al. [29] summarized key aspects of the thermal behavior of DBD plasma actuators. From an energy-conversion standpoint, plasma-based flow control has often been viewed as relatively "inefficient," since a substantial portion of the supplied electrical power is dissipated as heat rather than converted into useful mechanical work [20], [30]. Nevertheless, this thermal output can be advantageous for aircraft icing mitigation and has therefore been actively explored for anti-/de-icing applications [16], [31]–[37]. Because of the heat released during operation, the temperature of the dielectric surface can rise markedly while the actuator is energized [30], primarily due to heat transfer from the plasma region to the surface [38], [39]. During discharge, the gas temperature within the plasma zone may increase significantly; for example, rotational temperatures on the order of 400 K have been reported near the edge of the exposed electrode [40]. Rodrigues et al. [41] also presented a thermodynamic analysis of the dielectric layer response in plasma actuators. In addition, plasma actuators incorporating advanced dielectric concepts have been proposed, including composite-ceramic dielectrics with improved high-temperature endurance [42] and polymer-based electrodes electro-active movement to promote ice shedding [43]. Experimental demonstrations of DBD plasma for icing mitigation have included tests in cold-chamber environments [14] and icing wind tunnel studies on simplified geometries such as cylinders [15] and airfoils [16]. Liu et al. [32] compared DBD plasma heating with conventional electro-thermal methods and reported that AC-driven DBD actuation can provide comparable or improved anti-icing performance relative to a traditional heating film. Another study revealed the effect of plasma actuator layout, showing that streamwise configuration demonstrated better anti-icing results [37]. Furthermore, Hui et al. [44] analyzed the flow field during plasma actuation for anti-/de-icing. Recently, more fundamental studies were conducted by Ahumada Lazo and Liu [45], which revealed the transient hydrodynamics of droplets impinging on surfaces with DBD plasma.

While previous studies demonstrated thermal or momentum effects of DBD plasma actuation, simultaneous measurement of induced thrust and thermal response has not been systematically quantified. In this study, we carried out a parametric investigation to examine the thermodynamic performance of AC-driven DBD plasma actuators pertinent to icing mitigation. Specifically, we assessed how the applied voltage, dielectric material, and dielectric thickness influence power draw and the associated thermal energy release. The thermal characteristics of AC-DBD in still air were captured using an infrared (IR) camera. In parallel, thrust was measured at the same operating conditions to provide a direct characterization of the actuator's mechanical output.

2 Experimental setup

All tests were conducted on a flat plate in still air, in a climate-controlled laboratory maintained at a room temperature of 22 °C and a relative humidity of 40 %. The DBD plasma actuators were mounted on an acrylic base plate. Copper tape with a thickness of 70 μm was applied to the plate to serve as the grounded electrode. A second copper strip, left exposed (≈70 μm thick and ≈95 mm long), was positioned adjacent to the edge of the ground electrode and electrically isolated from it using different dielectric layers. The desired dielectric thicknesses for Kapton and PVC were obtained by laminating several layers of commercially available film with single-layer thicknesses of ∼90 μm for Kapton and ∼70 μm for PVC, while PTFE was used as single-layer sheets commercially available at the selected thicknesses. Plasma discharge was initiated by applying a high-voltage signal to the exposed electrode. A schematic of the actuator configuration is provided in Figure 1.

The DBD plasma actuators were driven by a high-voltage AC power supply (Nanjing Suman, CTP-2000 K). The applied voltage and discharge current were measured using a Tektronix P6015 high-voltage probe and a

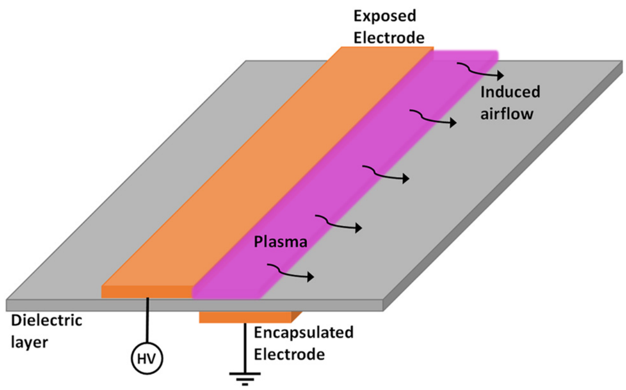

Figure 1: Layout of the dielectric barrier discharge actuator.

Pearson 2877 current probe, respectively. The voltage and current measurements carry the specified accuracies of the probes e.g., ±2 % for the Tektronix P6015 (1,000:1 attenuation; 20 kV DC/40 kV peak measurement range; DC–75 MHz bandwidth) and +1 %/−0 % for the Pearson 2877 (1 V/A sensitivity; 100 A peak; 300 Hz–200 MHz bandwidth). Both signals were recorded with a Tektronix MDO3102 mixed-domain oscilloscope. The waveforms were digitized at a sample rate of 10 MS/s with a vertical resolution of 8 bits.

The electrical power consumption was then determined from the measured voltage–current data using:

$$P = \frac{1}{T}\int_{0}^{T} V(t) \times I(t)\mathrm{d}t \tag{1}$$

where $V(t)$ and $I(t)$ denote the time-resolved voltage and current supplied to the plasma actuator. Here, T is the sampling interval used for the calculation, chosen to include approximately eight periods of the applied AC waveform. Figure 2 shows a typical voltage and current trace. The applied voltage is nearly sinusoidal, whereas the current consists of a low-amplitude sinusoidal component – the capacitive (displacement) current of the actuator – superimposed with trains of sharp spikes in both half-cycles. The sinusoidal component of the current leads the voltage by roughly a quarter of a cycle, as expected for a predominantly capacitive load [22]; the apparent displacement between the two signals therefore reflects the reactive character of the actuator rather than a delay in the discharge itself. The current spikes mark individual micro-discharges. The spikes during the positive-going half-cycle are stronger, while those during the negative-going half-cycle are weaker [22]. This asymmetry stems from the different electron sources in the two half-cycles: when the exposed electrode is negative, it acts as the cathode and readily emits electrons, producing numerous weak micro-discharges in a relatively uniform, glow-like discharge; when the exposed electrode is positive, electrons must instead be drawn from the weakly emitting dielectric surface, so breakdown occurs less frequently but through stronger, streamer-like micro-discharges [22], [23]. These micro-discharge events sustain the ionization responsible for both the electrohydrodynamic force production and the heat release of the actuator.

Surface temperature fields during plasma operation were measured using a FLIR A615 infrared (IR) camera (640 × 480 pixels; ±2 % accuracy). The camera was positioned facing the flat plate at a stand-off distance of 0.3 m. Image acquisition began at the same time as the plasma was initiated, and thermal data were recorded at 50 Hz.

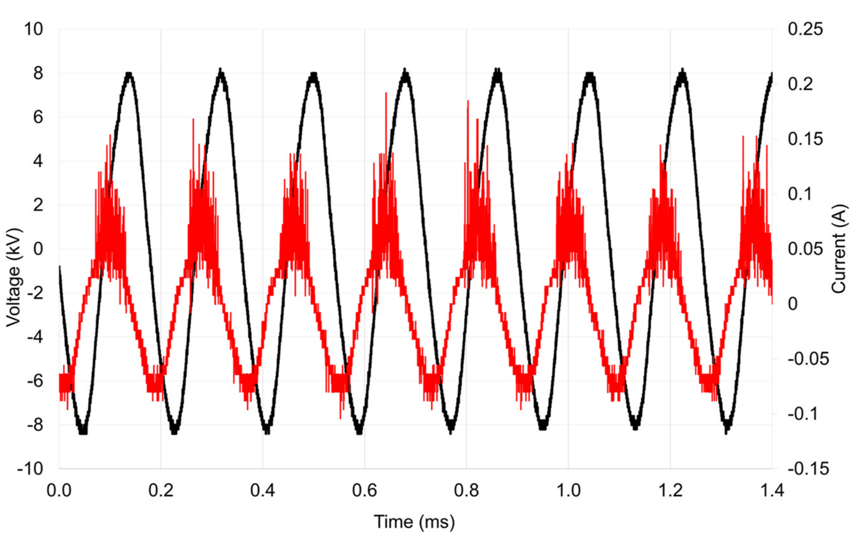

Figure 2: Representative voltage and current waveforms during plasma operation.

To correct for differences in surface emissivity, the camera emissivity settings were specified as $\varepsilon = 0.84$, 0.92, and 0.91 for Kapton, PTFE, and PVC, respectively. These values were obtained through *in-situ* calibration by matching IR readings with temperatures measured by thermocouples. In addition, the exposed copper electrode was covered with PVC tape to minimize reflections from the metallic surface.

Alongside the surface-temperature measurements, thrust was quantified concurrently using a Veritas M214 analytical balance with a resolution of 0.00098 mN. The flat plate was mounted vertically on the balance for the force tests. Electrodes were connected to the power source via 0.05 mm diameter copper wires, which were kept slack to minimize any parasitic tension effects on the measured thrust. The balance output was logged to a computer at 7 Hz, and the recorded force signal was subsequently time-averaged. Electromagnetic interference produced by the high-voltage discharge was successfully mitigated by shielding and grounding of the data cable between the balance and the computer. In addition, the plasma circuit was electrically insulated from the measurement equipment, and all measurement instruments were tested prior to the experiments under various DBD discharge conditions to verify that the readings were free of electromagnetic interference. A schematic of the overall experimental arrangement is provided in Figure 3.

3 Measurement results and discussions

The measurements below are organized to build from cause to effect. First, the influence of the governing parameters (applied voltage, dielectric material, and dielectric thickness) on surface heating is quantified and interpreted through the electrical power delivered to the discharge, which Equations (3)–(5) relate to those same parameters. The simultaneous thrust and temperature measurements are then used to examine how the delivered power is partitioned between mechanical (momentum) output and thermal output, and how this partitioning changes across the glow-to-streamer transition.

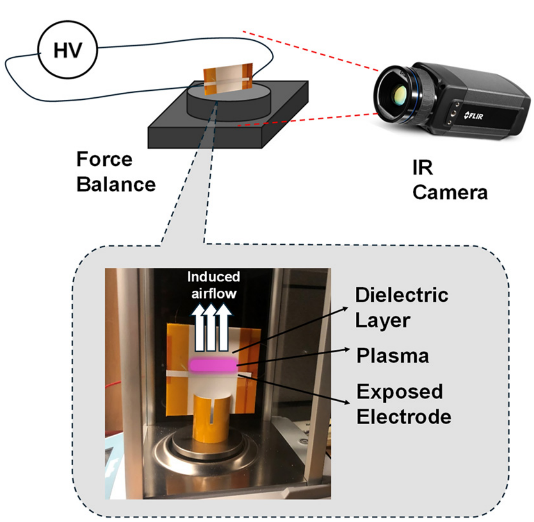

Figure 3: Experimental setup.

3.1 Influence of dielectric material, thickness, and applied voltage

The heat released by DBD plasma actuation would differ under different plasma actuator parameters such as voltage or dielectric layer properties. A part of the released heat would eventually transfer to the dielectric surface of the plasma actuator. The surface heating produced by DBD plasma actuation was evaluated on a flat plate in still air for several test conditions. The different experimental groups and their corresponding operating parameters are summarized in Table 1. The effect of voltage input was investigated on a 0.80 mm thick Kapton dielectric layer. The effect of dielectric layer type was explored under 12 kV peak-to-peak AC voltage, while the thickness of the layers was 0.35 mm. The effect of the thickness was investigated on PTFE layers with 15 kV voltage. The AC frequency was kept constant at 6 kHz to isolate the effects of dielectric material and thickness within the available power-supply operating envelope. We acknowledge that changing dielectric properties alters the equivalent capacitance and may shift optimal operating frequency; therefore, the present results should be

Table 1: Test cases.

Case set	Dielectric material	Thickness (mm)	Voltage (kV)
Influence of voltage	Kapton	0.80	2.0 4.0 6.0 12.0 15.0 20.0
Influence of dielectric material	Kapton PVC PTFE	0.35	12.0
Influence of dielectric thickness	PTFE	0.35 0.80 1.58 3.17 6.35	15.0

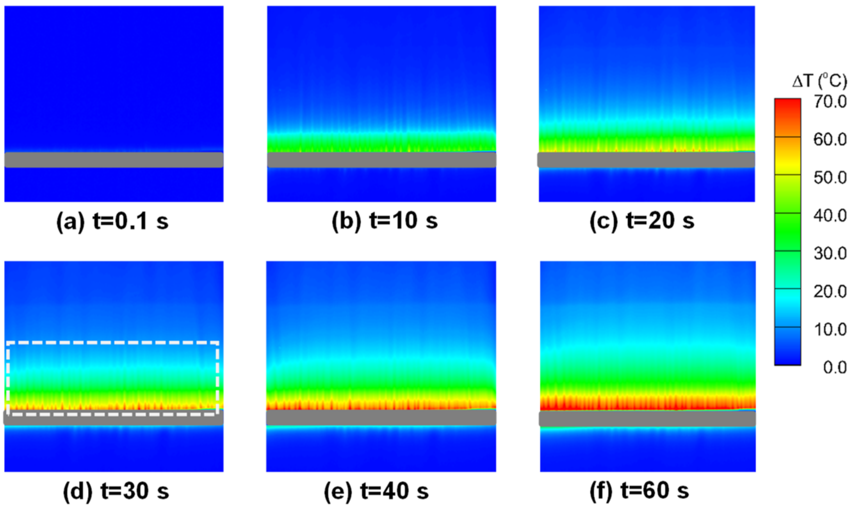

Figure 4: Temporal progression of the surface-temperature field. $V = 20$ kV, $f = 6$ kHz, 0.8 mm Kapton dielectric layer.

interpreted as a controlled comparison at fixed frequency rather than a global optimization over frequency. During the experiments the surface temperature was measured by IR imaging.

Figure 4 presents the temporal development of surface-temperature fields on the actuator dielectric for an operating condition of 20 kV and 6 kHz. In the IR frames, the exposed electrode region was intentionally obscured with a gray stripe. Initially, the dielectric surface was essentially at ambient temperature. Once the actuator was energized, the dielectric beneath the plasma region heated up rapidly. With continued operation, the warmed area spreads downstream from the discharge zone due to heat conduction within the solid and convective transport associated with the downstream-moving heated gas layer. The highest temperatures occur near the edge of the exposed electrode, where the surface temperature rises by more than 70 °C after 60 s.

Surface temperatures on the flat plate were recorded for multiple AC-DBD voltage levels. A 0.8 mm Kapton layer was selected as the dielectric because of its relatively high thermal resistance. Figure 5a reports the mean temperature rise over the region marked by the white dashed box in Figure 4d, extending approximately 20 mm downstream from the edge of the exposed electrode. This 20 mm interrogation window was chosen because it bounds the region where plasma-induced heating was consistently measurable for all test conditions; as shown by the

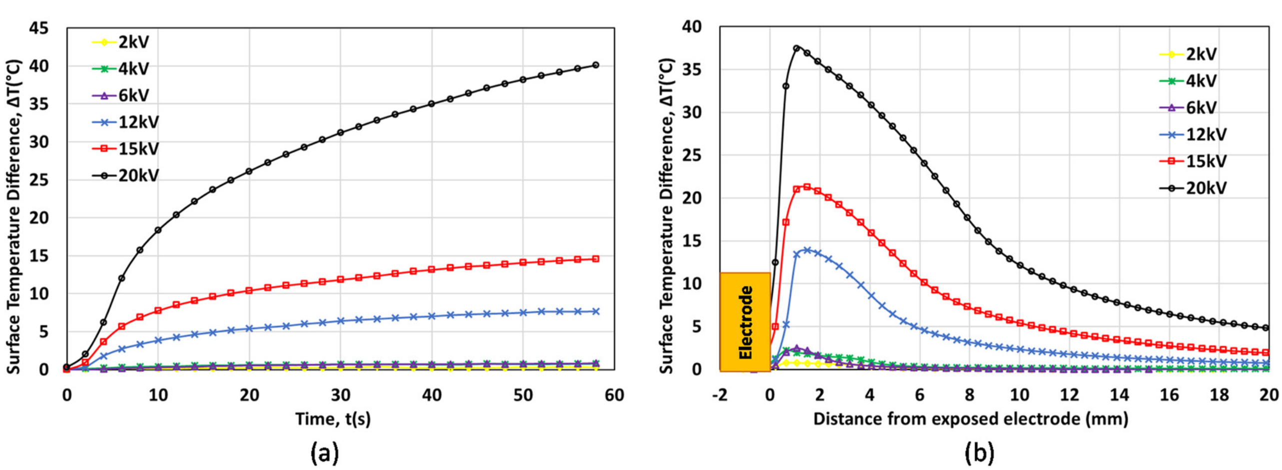

Figure 5: Influence of voltage input. (a) Surface temperature increment versus time, (b) spanwise-averaged temperature profile after 10 s of plasma actuation.

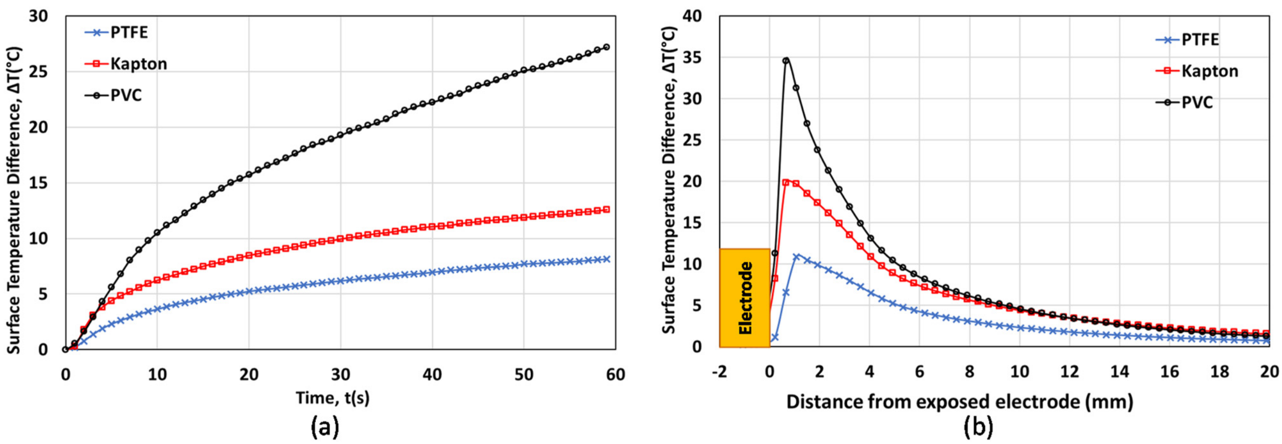

Figure 6: Influence of dielectric material. (a) Surface temperature increment versus time; (b) spanwise-averaged temperature profile after 10 s of plasma actuation.

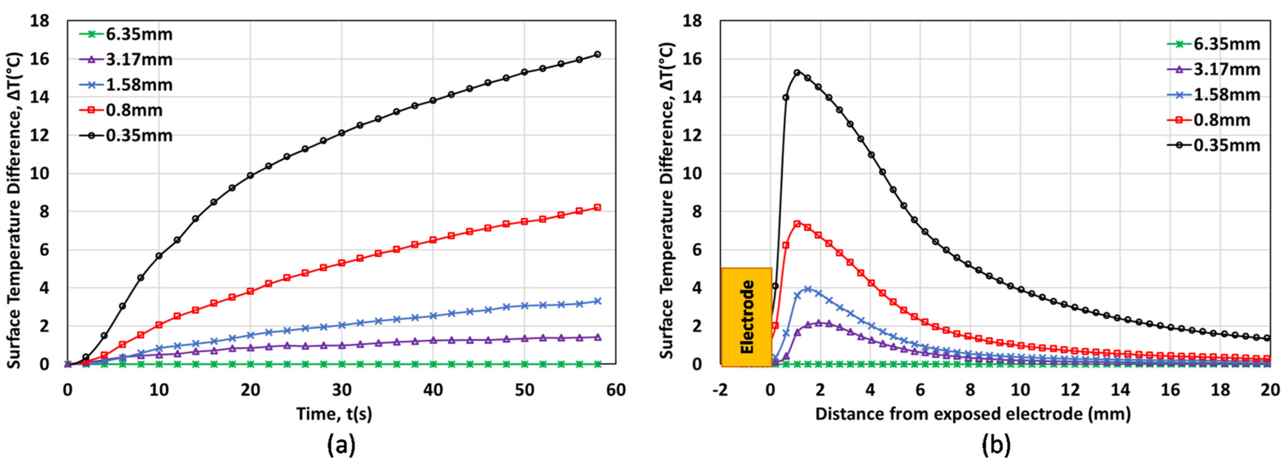

Figure 7: Influence of dielectric layer thickness. (a) Surface temperature increment versus time; (b) spanwise-averaged temperature profile after 10 s of plasma actuation.

spanwise-averaged profiles (Figures 5b, 6b and 7b), the temperature rise decays rapidly with downstream distance: at 10 s after the actuation onset, the spanwise-averaged temperature rise at 20 mm downstream has already dropped to below 13 % of its near-electrode peak for every test condition (e.g., 4.9 °C versus a 37.5 °C peak at 20 kV, and less than 0.1 °C for 2–6 kV). Extending the window farther downstream would therefore mainly add weakly heated area and dilute the area-averaged temperature, weakening the comparison between test conditions. Figure 5b provides the corresponding spanwise-averaged temperature distributions. As shown in Figure 5, the lowest excitation levels (2–6 kV) produced negligible heating: the time-dependent temperature rise remained small, and the warming was confined to a narrow zone near the exposed-electrode edge, with essentially no increase farther downstream (Figure 5b). In contrast, moderate-to-high voltages (12–15 kV) yielded a more pronounced thermal response. The area-averaged temperature increased rapidly immediately after actuation began and then approached a quasi-steady value more gradually. The maximum heating still occurred close to the exposed-electrode edge, but with substantially larger peak values (Figure 5b). At the highest voltage tested (20 kV), the mean temperature rise was much steeper, exceeding 40 °C within about 60 s, consistent with a substantially higher thermal energy deposition. The peak increase reached 38 °C near the electrode, and even at 20 mm downstream the surface temperature rose by about 5 °C after 10 s of actuation.

Surface temperatures were compared for three dielectric materials – Kapton, PTFE, and PVC – tested under identical operating conditions (12 kV, 6 kHz). For consistency, the thickness of each dielectric layer was fixed at 0.35 mm. Figure 6a presents the time history of the area-averaged surface temperature, whereas Figure 6b shows the spatially averaged temperature rise as a function of distance from the exposed-electrode edge at 10 s after actuation begins. As indicated in Figure 6, PTFE and Kapton exhibit relatively modest heating, with surface-temperature increases of about 8 °C and 12 °C, respectively, after 60 s. In contrast, PVC experiences substantially stronger heating, reaching an increase of approximately 27 °C over the same period. While the Kapton and PTFE cases gradually approach a steady value, the PVC surface continues to warm more rapidly and to a higher level. The profiles in Figure 6b further show that, at 10 s, the peak temperature rise near the electrode is approximately 15 °C for PTFE, 20 °C for Kapton, and 35 °C for PVC.

Figure 7 illustrates how dielectric thickness affects surface heating, shown both as a time history and as a spatial distribution measured away from the electrode edge. These tests were conducted at 15 kV and 6 kHz while varying only the thickness of the PTFE (Teflon) dielectric. Overall, reducing the dielectric thickness led to stronger heating, producing higher surface temperatures over time and larger temperature rises farther downstream from the electrode. At the largest thickness tested (6.35 mm), no visible discharge was observed even though the applied voltage was 15 kV, and the surface temperature did not change measurably. These observations indicate that the heating of the dielectric surface is primarily driven by thermal energy deposited during plasma discharge. From a control-oriented standpoint, the area-averaged temperature histories in Figures 5a, 6a and 7a are well approximated by a first-order (single-time-constant) step response,

$$\Delta T(t) \approx \Delta T_\infty \left[1 - e^{-t/\tau}\right] \tag{2}$$

in which both the steady-state rise, $\Delta T_{\infty,}$ and the time constant, τ, vary systematically with the operating parameters. The measured time histories therefore lend themselves to parameter-dependent, low-order dynamic models of the type used in systems identification, which could serve as plant models for closed-loop control of plasma-based ice protection; developing such models is a promising direction for future work.

Manley [46] introduced a power-estimation approach for dielectric barrier discharges based on Lissajous plots in 1943, in which the energy delivered to the discharge over a single AC cycle is obtained from the area enclosed by the voltage–charge (V–Q) curve. In the present study, the power consumption was determined directly from the time-resolved voltage and current measurements using Equation (1). Manley's framework is invoked here to interpret the parametric dependence of the measured power on the applied voltage, dielectric thickness, and dielectric permittivity, as expressed by Equations (3)–(5); as shown below, the measured trends are consistent with this dependence. Accordingly, the discharge power can be expressed as [46]–[48]:

$$P = 4f\frac{C_d^2}{C_d + C_a}V_{\min}\left(V_{\max} - V_{\min}\right) \tag{3}$$

Here, f denotes the excitation frequency, $V_{\min}$ is the minimum applied voltage required to initiate discharge, $V_{\max}$ is the peak applied voltage, C_a and C_d represent the effective capacitances of the air gap and the dielectric layer, respectively. C is defined as:

$$C = \kappa\,\varepsilon_0\frac{A}{d} \tag{4}$$

where κ is dielectric constant, ε_0 is vacuum permittivity, A is effective electrode area and d is dielectric layer thickness. Substituting the expression for C into equation (3) yields the plasma-actuator power consumption given in equation (5):

$$P = 4f\frac{\left(\kappa_d\varepsilon_0\frac{A}{d_d}\right)^2}{\kappa_d\varepsilon_0\frac{A}{d_d} + \kappa_a\varepsilon_0\frac{A}{d_a}}V_{\min}\left(V_{\max} - V_{\min}\right) \tag{5}$$

Equation (5) indicates that the discharge power rises as voltage, $V_{\max}$, and dielectric constant, κ_d, increase, whereas a thicker dielectric layer, d_d, tends to lower the electrical power consumption. This behavior is reflected in Figure 8, which shows that variations in parameters such as voltage, thickness and permittivity produce comparable trends in both power and surface temperature. In other words, operating conditions that require more electrical power also lead to greater heat release, resulting in a higher surface temperature. The uncertainty of the results in Figure 8 stems from the accuracies of the measurement instruments: the power-per-length values carry the combined accuracy of the voltage and current probes (±2 % for the Tektronix P6015 and +1 %/−0 % for the Pearson 2877), while the area-averaged surface temperatures carry the ±2 % of reading accuracy of the FLIR A615 IR camera.

3.2 Relation between momentum transfer and thermal energy release

A DBD plasma actuator incorporating a 3.17 mm PTFE (Teflon) dielectric was evaluated under AC excitation at 8 kHz while the peak voltage was varied from 10 to 40 kV. The use of a relatively thick dielectric enabled operation over this broad voltage range without actuator failure. Surface temperature fields were captured using IR thermography, and the actuation-induced thrust was recorded simultaneously with the high-resolution balance.

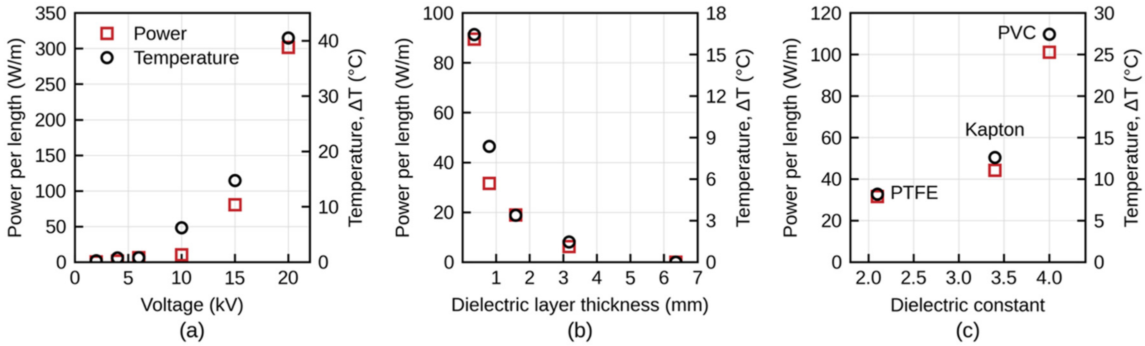

Figure 8: Power consumption and area-averaged surface temperature after 60 s of actuation plotted against (a) voltage input, (b) dielectric layer thickness (c) dielectric constant.

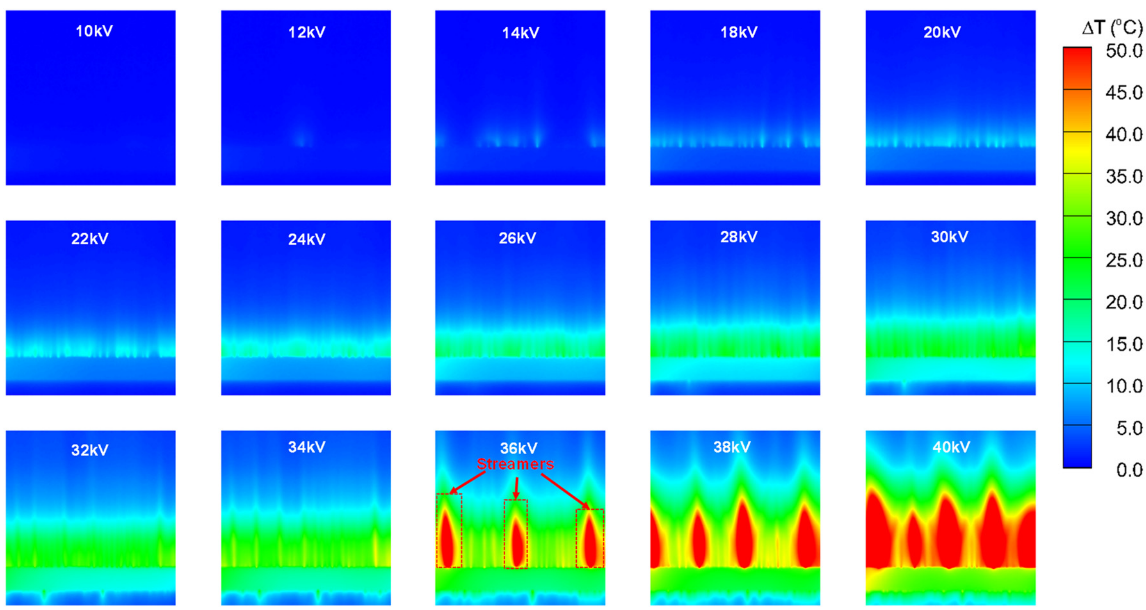

Figure 9: Surface temperature maps of the flat plate after 60 s of actuation for various applied voltages.

Figures 9 and 10 summarize the thermal response of the flat plate after 60 s of actuation at different applied voltages. Figure 9 presents the surface temperature maps, and Figure 10 provides the corresponding spanwise-averaged temperature distributions along the streamwise direction. Both figures show that, at the lower voltage levels, the discharge is relatively weak and the resulting surface heating is limited. In all cases, the maximum temperature occurs near the exposed-electrode edge and then decays downstream. For voltages up to 34 kV, the temperature field is nearly uniform across the span, consistent with a spatially continuous discharge operating in the glow regime. When the voltage is increased to 36 kV and above, discrete hot spots appear on the surface. These localized peaks are associated with the onset of streamer filaments in the plasma. The temperature maps in Figure 9 thus serve as a spatial diagnostic of the discharge regime: spanwise uniformity of the surface-temperature field indicates a diffuse glow discharge, whereas the appearance and growth of discrete hot spots identify the onset and intensification of streamer filaments [49], [50] – information that spanwise-averaged profiles alone cannot provide.

Figure 11 compares the mean surface-temperature rise measured after 60 s of actuation with the corresponding thrust levels for the range of applied voltages, while Figure 12 replots the same quantities against the electrical power input. Because each thrust value represents an average over a time series, the associated variability is indicated by the error bars in Figure 11. As shown in Figure 11, surface heating and thrust increase in a similar manner as long as the discharge remains in the glow mode. Once streamer filaments appear (approximately 36–40 kV), the trends diverge:

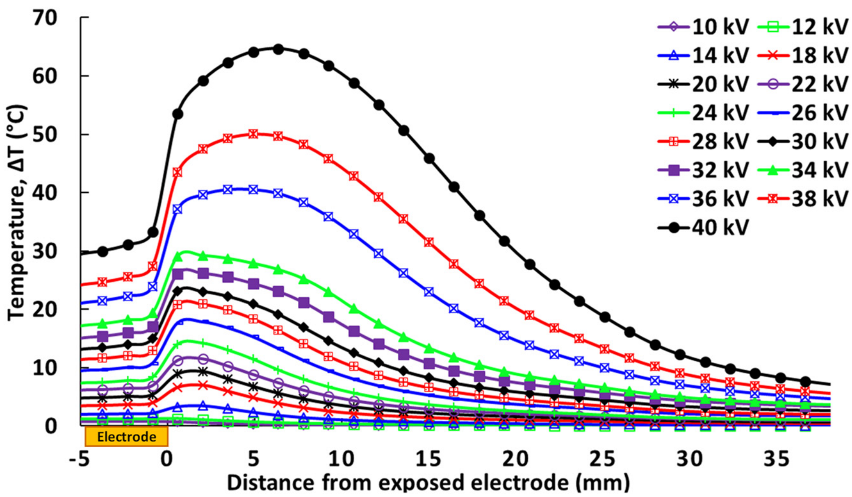

Figure 10: Streamwise temperature distributions (spanwise averaged) measured after 60 s of actuation at various voltage input.

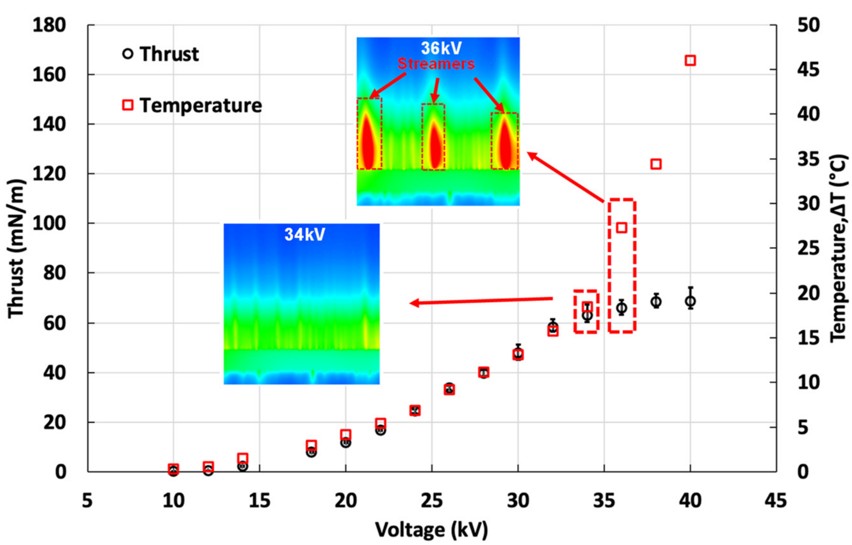

Figure 11: Area-averaged surface temperature after 60 s of actuation and corresponding thrust versus applied voltage input.

the average surface temperature rises sharply, whereas the measured thrust shows little or no additional increase. Consistently, Figure 12 indicates that both temperature and thrust scale approximately linearly with power consumption below 36 kV, but after the transition to the filamentary regime, further increases in power do not translate into greater thrust and instead manifest primarily as enhanced heating.

When plasma is in the glow regime, the fractions of the input power converted into thermal output and kinetic output remain approximately constant. At sufficiently high applied voltage, the discharge becomes unstable and transitions toward a localized filamentary (streamer) mode, in which a localized, transient micro-discharge pattern is observed as bright, spatially concentrated filaments along the exposed-electrode edge. In this regime, streamer filaments constrain further thrust increase, even though the dissipated power continues to rise with increasing voltage [49], [50]. Additional electrical power is dissipated in enhanced Joule heating, while the net EHD body force does not increase proportionally; consequently, the measured net thrust component saturates within the uncertainty bounds, whereas surface heating continues to rise.

Quantifying the energetic transition across the saturation threshold reveals stark redirection of actuator's power budget. Prior to the onset of filamentary streamers, thermal dissipation rate was found to be 0.075 °C/(W/m), derived directly from the slope of a linear curve fit of the pre-saturation data (R^2 = 0.9945, denoted by the dashed red line). Crossing the 34 kV threshold triggers a regime

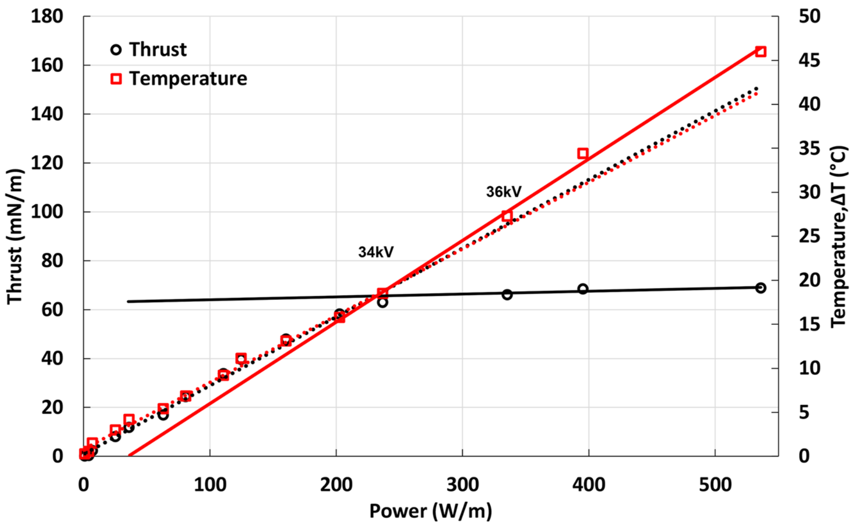

Figure 12: Area-averaged surface temperature after 60 s of actuation and corresponding thrust versus applied power input.

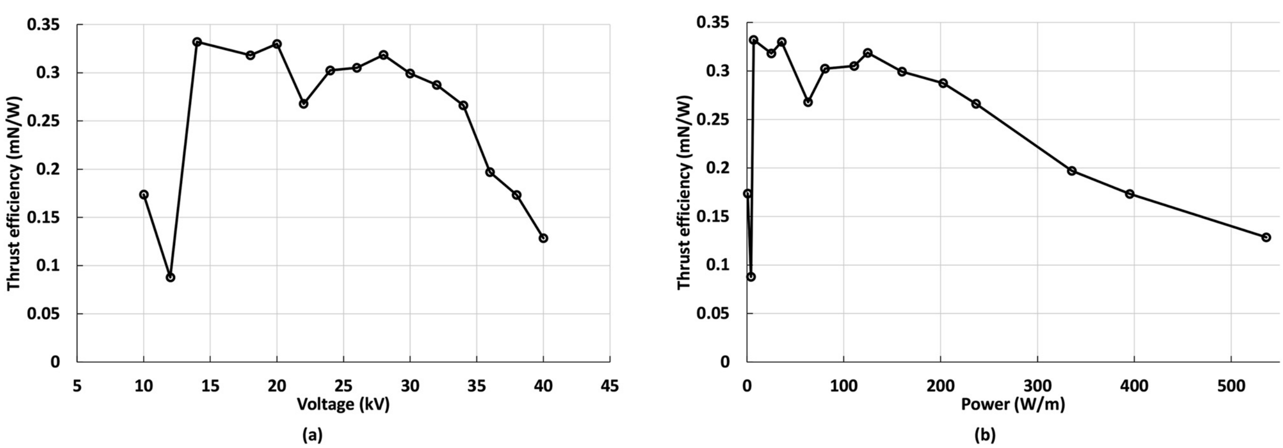

Figure 13: Thrust efficiency versus applied (a) voltage and (b) power input.

transition to a steeper linear profile. Within this post-saturation domain ($R^2 = 0.9960$, denoted by the solid red line), the incremental thermal dissipation rate rises to 0.0933 °C/(W/m). This rise in the thermal dissipation rate represents 24.4 % increase in surface heating. The results indicate that the onset of streamer filaments shifts the added power primarily into heat release. After streamers form, a substantially larger portion of the input electrical energy is dissipated as thermal energy rather than contributing to thrust output. Each temperature data point used in these fits is the spatial average of the IR-measured surface temperature over the fixed interrogation window described above (extending 20 mm downstream of the exposed-electrode edge), evaluated after 60 s of actuation. The two fits were obtained by ordinary least squares, which presumes a linear mean response, independent errors, homoscedasticity, and approximately normally distributed residuals. Within each regime, the residuals were examined and show no systematic trend with power, supporting the linearity and constant-variance assumptions. The reported R^2 values should be read as descriptive measures of goodness of fit rather than inferential statistics.

Figure 13 illustrates the electromechanical performance of the AC-DBD plasma actuator, specifically plotting the thrust efficiency (η) as a function of (a) applied peak-to-peak voltage and (b) electrical power input. This efficiency metric quantifies the mechanical force (T) generated per unit of active electrical power input (P). It is calculated similar to the “fluid mechanic effectiveness” as in Kriegseis et al. [51]:

$$\eta = \frac{T}{P} \tag{6}$$

At low voltages (10 kV–14 kV), the efficiency exhibits sharp fluctuations. Near the breakdown voltage of air, the plasma discharge is not yet fully continuous or uniform across the electrode span, leading to a weak, unsteadily developed ionic wind. Following this initialization phase, a stable operational plateau is established between 14 kV and 34 kV where the efficiency peaks and stabilizes between 0.27 mN/W and 0.33 mN/W. Within this optimized envelope, the actuator operates in a highly uniform, diffuse glow discharge regime, maintaining a linear scaling between thrust and input power. Crossing the 34 kV saturation threshold initiates a steep, continuous decay in thrust production efficiency, because the total thrust output plateaus completely beyond this threshold. This decay illustrates that any power injected past the saturation point is entirely diverted away from momentum generation and is instead absorbed by thermal dissipation, micro-discharge filamentation, and substrate dielectric losses. The plateau values of 0.27–0.33 mN/W fall within the range of effectiveness reported for AC-DBD actuators by Kriegseis et al. [51], and the overall shape of Figure 13 – a low-voltage initialization region (<14 kV), a broad plateau in the glow regime (14 kV–34 kV), and a decay beyond the streamer transition (>34 kV) – is consistent with the established picture that the electrohydrodynamic body force is generated most efficiently by a uniform glow discharge, while filamentary micro-discharges dissipate energy mainly as heating [49], [50].

4 Conclusions

This work presents a parametric experimental campaign of the thermal behavior of AC-driven DBD plasma actuators. Experiments were carried out at ambient conditions with a flat-plate arrangement in still air. Infrared (IR) thermography was employed to capture surface-temperature fields for a range of operating conditions, enabling the thermal response of the actuator to be quantified. The influence of applied voltage, dielectric material, and dielectric thickness was examined in a systematic manner. In parallel, the thrust generated by the plasma-induced ionic wind was measured with an analytical balance, allowing the coupling between thermal output and momentum (kinetic) production to be assessed.

The results show that the surface-heating response of AC-DBD actuation is strongly governed by operating and material parameters, including the applied voltage as well as the dielectric thickness and material type. Higher voltage and larger dielectric permittivity increase the electrical power delivered to the discharge, whereas increasing the dielectric thickness reduces the power. Since the deposited power controls the heat released by the plasma, these variations translate directly into changes in surface temperature.

The concurrent thrust and thermal measurements further indicate that, in the glow-discharge regime, both heat release and momentum production scale approximately linearly with plasma power and exhibit the same overall trend. As the input power is raised, the discharge transitions from a diffuse glow to localized streamer filaments; beyond this point, a larger fraction of the power is dissipated as heat, while thrust no longer increases and instead levels off. The distinct energetic shift triggered by the streamer transition dictates mutually exclusive operational strategies depending on whether the AC-DBD actuator is deployed for aerodynamic flow control or thermal anti-icing purposes. For boundary layer flow control, operating the actuator beyond the electromechanical saturation threshold is fundamentally counterproductive. In this high-voltage domain, any additional electrical power fails to generate further electrohydrodynamic body force. Therefore, flow control configurations must be kept within the uniform glow discharge regime, where momentum injection scales optimally with power input. Conversely, for aircraft anti-icing applications, the post-saturation filamentary regime represents the ideal operational envelope since any power addition is directed into surface as heat.

Overall, the present dataset provides a regime-dependent trade-off between thermal output and momentum production for AC-DBD actuators in quiescent air. These results can support actuator parameter selection depending on whether the intended objective prioritizes surface heating or flow-control authority and can be extended to design more effective plasma-based ice protection for aircraft.

Research ethics: Not applicable.
Informed consent: Not applicable.
Author contributions: All authors have accepted responsibility for the entire content of this manuscript and approved its submission. Hui Hu conceptualized the study, provided supervision, participated in the analysis, and secured the funding. Cem Kolbakir also contributed to the conceptualization, conducted the experiments, performed the data analysis, and prepared the initial draft of the manuscript. Haiyang Hu and Yang Liu participated in the execution of the experiments and contributed to the data analysis.
Use of Large Language Models, AI and Machine Learning Tools: During the preparation of this work the author(s) used Google Gemini 3.5 in order to improve grammar, clarity, and readability of the manuscript text. After using this tool/service, the author(s) reviewed and edited the content as needed and take(s) full responsibility for the content of the published article.

Conflict of interest: The authors state no conflict of interest.
Research funding: The research work is supported by National Science Foundation (NSF) under award numbers of CBET-1935363 and TI-2140489.
Data availability: The raw data can be obtained on request from the corresponding author.

References

[1] M. B. Bragg, G. M. Gregorek, and J. D. Lee|, "Airfoil aerodynamics in icing conditions," *J. Aircraft*, vol. 23, no. 1, 1986, https://doi.org/10.2514/3.45269.
[2] S. D. Green, "The Icemaster database and an analysis of aircraft aerodynamic icing accidents and incidents," Federal Aviation Administration, Atlantic City, NJ, USA, Tech. Rep. DOT/FAA/TC-14/44, 2015.
[3] M. G. Potapczuk, "Aircraft icing research at NASA Glenn research center," *J. Aerosp. Eng.*, vol. 26, no. 2, pp. 260—276, 2013, https://doi.org/10.1061/(ASCE)AS.1943-5525.0000322.
[4] S. K. Thomas, R. P. Cassoni, and C. D. MacArthur, "Aircraft anti-icing and de-icing techniques and modeling," *J. Aircr.*, vol. 33, no. 5, pp. 841—854, 1996, https://doi.org/10.2514/3.47027.
[5] L. M. Nicolai, C. A. Martin, and J. C. Puttt, "Advanced pneumatic impulse ice protection system (PUP) for aircraft," *J. Aircr.*, vol. 29, no. 4, pp. 714—716, 1991, https://doi.org/10.2514/3.46227.
[6] M. P. C. Pellissier, W. G. Habashi, and A. Pueyo, "Optimization via FENSAP-ICE of aircraft hot-air anti-icing systems," *J. Aircr.*, vol. 48, no. 1, 2011, https://doi.org/10.2514/1.C031095.
[7] J. M. Brown, S. Raghunathan, J. K. Watterson, A. J. Linton, and D. Riordon, "Heat transfer correlation for anti-icing systems," *J. Aircr.*, vol. 39, no. 1, 2002, https://doi.org/10.2514/2.2896.
[8] F. Morency, F. Tezok, and I. Paraschivoiu, "Anti-icing system simulation using CANICE," *J. Aircr.*, vol. 36, no. 6, pp. 999—1006, 1999, https://doi.org/10.2514/2.2541.
[9] R. Henry, "Development of an electrothermal De-icing/Anti-icing model," in *30th Aerospace Sciences Meeting & Exhibit*, Reno, NV, USA, American Institute of Aeronautics and Astronautics, 1992.
[10] G. A. L. Da Silva, O. D. M. Silvares, and E. J. D. G. J. Zerbini, "Water film breakdown and rivulets formation eects on thermal anti-ice operation simulation," in *9th AIAA/ASME Joint Thermophysics and Heat Transfer Conference*, San Francisco, California, USA, American Institute of Aeronautics and Astronautics, 2006.
[11] A. G. Kraj and E. L. Bibeau, "Phases of icing on wind turbine blades characterized by ice accumulation," *Renew. Energy*, vol. 35, no. 5, pp. 966—972, 2010, https://doi.org/10.1016/j.renene.2009.09.013.
[12] R. M. Waldman, H. Li, H. Guo, L. Li, and H. Hu, "An experimental investigation on the effects of surface wettability on water runback and ice accretion over an airfoil surface," in *8th AIAA Atmospheric and Space Environments Conference*, Washington, D.C., USA, American Institute of Aeronautics and Astronautics, 2016.
[13] P. Zhang and F. Y. Lv, "A review of the recent advances in superhydrophobic surfaces and the emerging energy-related applications," *Energy*, vol. 82, pp. 1068—1087, 2015, https://doi.org/10.1016/j.energy.2015.01.061.
[14] J. Van Den Broecke, *De-icing Using ns-DBD Plasma Actuators*, Delft, The Netherlands, Delft University of Technology, 2016.
[15] J. Cai, Y. Tian, X. Meng, X. Han, D. Zhang, and H. Hu, "An experimental study of icing control using DBD plasma actuator," *Exp. Fluids*, vol. 58, no. 8, 2017, https://doi.org/10.1007/s00348-017-2378-y.
[16] W. Zhou, Y. Liu, H. Hu, H. Hu, and X. Meng, "Utilization of thermal effect induced by plasma generation for aircraft icing mitigation," *AIAA J.*, vol. 56, no. 3, 2018, https://doi.org/10.2514/1.J056358.
[17] Y. Liu, C. Kolbakir, H. Hu, and H. Hu, "A comparison study on AC-DBD plasma and electrical heating for aircraft icing mitigation," in *AIAA SciTech Forum*, Florida, Kissimmee, 2018.
[18] F. Rodrigues, M. Abdollahzadehsangroudi, J. Nunes-Pereira, and J. Páscoa, "Recent developments on dielectric barrier discharge (DBD) plasma actuators for icing mitigation," *Actuators*, vol. 12, no. 1, 2023, Art. no. 5, https://doi.org/10.3390/act12010005.
[19] T. C. Corke, C. L. Enloe, and S. P. Wilkinson, "Dielectric barrier discharge plasma actuators for flow control *," *Annu. Rev. Fluid. Mech.*, vol. 42, pp. 505—529, 2010, https://doi.org/10.1146/annurev-fluid-121108-145550.
[20] E. Moreau, "Airflow control by non-thermal plasma actuators," *J. Phys. D Appl. Phys.*, vol. 40, no. 3, p. 605, 2007, https://doi.org/10.1088/0022-3727/40/3/S01.
[21] T. C. Corke, M. L. Post, and D. M. Orlov, "Single dielectric barrier discharge plasma enhanced aerodynamics: Physics, modeling and applications," *Exp. Fluids*, vol. 46, no. 1, pp. 1—26, 2009, https://doi.org/10.1007/s00348-008-0582-5.
[22] N. Benard and E. Moreau, "Electrical and mechanical characteristics of surface AC dielectric barrier discharge plasma actuators applied to airflow control," *Exp. Fluids*, vol. 55, no. 11, 2014, https://doi.org/10.1007/s00348-014-1846-x.
[23] C. L. Enloe, T. E. Mclaughlin, R. D. Vandyken, K. D. Kachner, E. J. Jumper, and T. C. Corke, "Mechanisms and responses of a single dielectric barrier plasma actuAtor: Plasma morphology," *AIAA J.*, vol. 42, no. 3, 2004, https://doi.org/10.2514/1.2305.
[24] M. Post and T. Corke, "Separation control using plasma actuators - Stationary & oscillating airfoils," in *42nd AIAA Aerospace Sciences Meeting and Exhibit*, Reston, Virigina, American Institute of Aeronautics and Astronautics, 2004.
[25] E. Moreau, R. Sosa, and G. Artana, "Electric wind produced by surface plasma actuators: A new dielectric barrier discharge based on a three-electrode geometry," *J. Phys. D Appl. Phys.*, vol. 41, no. 11, 2008, Art. no. 115204, https://doi.org/10.1088/0022-3727/41/11/115204.
[26] D. Roupassov, A. Nikipelov, M. Nudnova, and A. Starikovskii, "Flow separation control by plasma actuator with nanosecond pulse periodic discharge," in *46th AIAA Aerospace Sciences Meeting and Exhibit*, Reston, Virigina, American Institute of Aeronautics and Astronautics, 2008.
[27] G. Correale, T. Michelis, D. Ragni, M. Kotsonis, and F. Scarano, "Nanosecond-pulsed plasma actuation in quiescent air and laminar boundary layer," *J. Phys. D Appl. Phys.*, vol. 47, no. 10, 2014, Art. no. 105201, https://doi.org/10.1088/0022-3727/47/10/105201.
[28] N. L. Aleksandrov, S. V. Kindysheva, M. M. Nudnova, and A. Y. Starikovskiy, "Mechanism of ultra-fast heating in a non-equilibrium weakly ionized air discharge plasma in high electric fields," *J. Phys. D Appl. Phys.*, vol. 43, no. 25, 2010, Art. no. 255201, https://doi.org/10.1088/0022-3727/43/25/255201.
[29] X. Zhang, Y. Zhao, and C. Yang, "Recent developments in thermal characteristics of surface dielectric barrier discharge plasma actuators driven by sinusoidal high-voltage power," *Chin. J.*

Aeronaut., vol. 36, no. 1, pp. 1–21, 2023, https://doi.org/10.1016/j.cja.2022.01.026.

[30] R. Joussot, D. Hong, H. Rabat, V. Boucinha, R. Weber-Rozenbaum, and A. Leroy-Chesneau, "Thermal characterization of a DBD plasma actuatoR: Dielectric temperature measurements using infrared thermography," in *40th Fluid Dynamics Conference and Exhibit*, Chicago, Illinois, USA, American Institute of Aeronautics and Astronautics, 2010.

[31] X. Meng, J. Cai, Y. Tian, X. Han, D. Zhang, and H. Hu, "Experimental study of deicing and anti-icing on a cylinder by DBD plasma actuation," in *47th AIAA Plasmadynamics and Lasers Conference AIAA*, Washington, D.C., USA, American Institute of Aeronautics and Astronautics, 2016.

[32] Y. Liu, C. Kolbakir, H. Hu, and H. Hu, "A comparison study on the thermal effects in DBD plasma actuation and electrical heating for aircraft icing mitigation," *Int. J. Heat Mass Transf.*, vol. 124, pp. 319–330, 2018, https://doi.org/10.1016/j.ijheatmasstransfer.2018.03.076.

[33] C. Kolbakir, Y. Liu, H. Hu, A. Y. Starikovskiy, and R. Miles, "An experimental investigation on the thermal effects of NS-DBD and AC-DBD plasma actuators for aircraft icing mitigation," in *AIAA SciTech Forum*, Florida, Kissimmee, 2018.

[34] Y. Liu, C. Kolbakir, H. Hu, H. Hu, and X. Meng, "An explorative study to use thermal effects of duty-cycled plasma actuations for aircraft icing mitigation," in *2018 Flow Control Conference, AIAA AVIATION Forum*, Atlanta, Georgia, USA, AIAA Paper 2018–3653, 2018, https://doi.org/10.2514/6.2018-3653.

[35] C. Kolbakir, H. Hu, Y. Liu, and H. Hu, "A hybrid Anti-/De-Icing strategy by combining NS-DBD plasma actuator and superhydrophobic coating for aircraft icing mitigation," in *AIAA SciTech 2019 Forum*, San Diego, California, USA, AIAA Paper 2019–0050, 2019, https://doi.org/10.2514/6.2019-0050.

[36] Y. Liu, C. Kolbakir, A. Y. Starikovskiy, Richard Miles, and H. Hu, "An experimental study on the thermal characteristics of NS-DBD plasma actuation and application for aircraft icing mitigation," *Plasma Sources Sci. Technol.*, vol. 28, no. 1, 2019, https://doi.org/10.1088/1361-6595/aaedf8.

[37] C. Kolbakir, H. Hu, Y. Liu, and H. Hu, "An experimental study on different plasma actuator layouts for aircraft icing mitigation," *Aerosp. Sci. Technol.*, vol. 107, 2020, Art. no. 106325, https://doi.org/10.1016/j.ast.2020.106325.

[38] S. A. Stanfield, J. Menart, C. Dejoseph, R. L. Kimmel, and J. R. Hayes, "Rotational and vibrational temperature distributions for a dielectric barrier discharge in air," *AIAA J.*, vol. 47, no. 5, pp. 1107–1115, 2009, https://doi.org/10.2514/1.37648.

[39] B. Dong, J. M. Bauchire, J. M. Pouvesle, P. Magnier, and D. Hong, "Experimental study of a DBD surface discharge for the active control of subsonic airflow," *J. Phys. D Appl. Phys.*, vol. 41, no. 15, 2008, Art. no. 155201, https://doi.org/10.1088/0022-3727/41/15/155201.

[40] S. Stanfield, J. Menart, C. DeJoseph, and R. Kimmel, "Rotational and vibrational termperatures for a dielectric barrier discharge in air using emission epectroscopy," in *38th AIAA Plasmadynamics and Lasers Conference*, Miami, Florida, USA, American Institute of Aeronautics and Astronautics, 2007.

[41] F. F. Rodrigues, J. C. Pascoa, and M. Trancossi, "Experimental analysis of dielectric barrier discharge plasma actuators thermal characteristics under external flow influence," *J. Heat Transfer*, vol. 140, no. 10, pp. 1–10, 2018, https://doi.org/10.1115/1.4040152.

[42] L. A. Mbanguine, F. F. Rodrigues, and J. C. Páscoa, "New electro-active polymers-based plasma actuators for simultaneous flow control and ice protection," *J. Fluids Eng.*, vol. 147, no. 7, 2025, https://doi.org/10.1115/1.4067786.

[43] K. O. Shvydyuk, F. F. Rodrigues, J. Nunes-Pereira, J. C. Páscoa, and A. P. Silva, "Thermal characterization of ceramic composites for optimized surface dielectric barrier discharge plasma actuators," *Actuators*, vol. 14, no. 3, 2025, https://doi.org/10.3390/act14030127.

[44] W. Hui, Z. Chen, J. Ma, and X. Meng, "Plasma-based anti-/de-icing: An experimental study utilizing supercooled water droplet image velocimetry," *Exp. Fluids*, vol. 66, no. 2, 2025, https://doi.org/10.1007/s00348-025-03960-y.

[45] J. A. Lazo and Y. Liu, "An experimental study on the spreading and fingering instability of droplet impacting on a surface with plasma discharge," *Phys. Fluids*, vol. 37, no. 9, 2025, https://doi.org/10.1063/5.0291036.

[46] T. C. Manley, "The electric characteristics of the ozonator discharge," *Trans. Electrochem. Soc.*, vol. 84, no. 1, pp. 83–96, 1943.

[47] K. Becker, U. Kogelschatz, K. Schoenbach, and R. Barker, *Non-Equilibrium Air Plasmas at Atmospheric Pressure*, Bristol, UK, Institute of Physics Publishing, 2004.

[48] X. Tao, R. Lu, and H. Li, "Electrical characteristics of dielectric-barrier discharges in atmospheric pressure air using a power-frequency voltage source," *Plasma Sci. Technol.*, vol. 14, no. 8, pp. 723–727, 2012, https://doi.org/10.1088/1009-0630/14/8/08.

[49] F. O. Thomas, T. C. Corke, M. Iqbal, A. Kozlov, and D. Schatzman, "Optimization of dielectric barrier discharge plasma actuators for active aerodynamic flow control," *AIAA J.*, vol. 47, no. 9, 2009, https://doi.org/10.2514/1.41588.

[50] I. Biganzoli, R. Barni, A. Gurioli, R. Pertile, and C. Riccardi, "Experimental investigation of filamentary and non-filamentary regimes in a surface dielectric barrier plasma actuator," in *Journal of Physics: Conference Series*, Bristol, UK, Institute of Physics Publishing, 2014.

[51] J. Kriegseis, A. Duchmann, C. Tropea, and S. Grundmann, "On the classification of dielectric barrier discharge plasma actuators: A comprehensive performance evaluation study," *J. Appl. Phys.*, vol. 114, no. 5, pp. 1–9, 2013, https://doi.org/10.1063/1.4817366.